Proton aurora in the cusp

H. U. Frey, S. B. Mende, T. J. Immel
SSL, University of California, Berkeley, USA

S. A. Fuselier, E. S. Claflin
Lockheed Martin ATC, Palo Alto, USA

J.-C. Gérard, B. Hubert
Université de Liège, Liège, Belgium

Short title: PROTON AURORA IN CUSP

Abstract. Frequently the FUV instrument on the IMAGE spacecraft observes intense ultraviolet emission from a localized dayside region poleward of the general auroral oval location. This emission is especially distinct in the Doppler shifted emission of hydrogen atoms produced by precipitating protons. We interpret this as a direct signature of proton precipitation into the cusp after reconnection of magnetospheric lobe field lines. This cusp signature appears only when the interplanetary magnetic field (IMF) has a positive northward B_z component. However, the intensity of the precipitation and hence the intensity of UV emission is not controlled by the magnitude of B_z but rather by the solar wind dynamic pressure. A statistical analysis of 18 cases observed in summer and fall 2000 shows good correlation between the UV intensity and the dynamic pressure, and between the location in local time and the IMF B_y component. A quantitative analysis of observations from all 3 FUV sub-instruments allows for an estimate of proton and electron energy fluxes during these times. In general, these estimates agree with results from in-situ measurements by spacecraft and show, that during these times protons may contribute significantly to the overall energy deposition into the cusp.

1. Introduction

The main objective of the IMAGE mission is to improve the understanding of magnetospheric processes. One signature of the interaction between the magnetosphere and ionosphere is the occurrence of aurora. Observations of the global aurora can provide important context information supplementing the direct imaging of the magnetosphere. Previously flown satellites have demonstrated the suitability of far ultra-violet imaging for remote sensing observations of auroral precipitation (see e.g. [*Frank and Craven,* 1988]). The major objective of the Far Ultraviolet Instrument (FUV) on IMAGE is the observation of global changes in the aurora accompanying large-scale changes in the magnetosphere [*Mende et al.,* 2000]. FUV consists of the imaging channels Wideband Imaging Camera (WIC) and the dual-channel Spectrographic Imager (SI-12 and SI-13). One feature of FUV is the capability for simultaneous observation in three different wavelength regions. Previously flown imagers had to change filters between exposures which introduced a temporal uncertainty when analysis involved comparison between distinct channels [*Torr et al.,* 1995].

Since its discovery by low-altitude polar orbiting satellites [*Burch,* 1968], the cusp has been known as the area where magnetosheath plasma could most easily access the lower altitude. Further statistical studies confirmed the localized nature of the cusp near local noon [see e.g. *Newell and Meng,* 1994] and established our knowledge about the morphology, dynamics, particle and optical signatures of the cusp [see e.g. *Reiff et al.,* 1977; *Woch and Lundin,* 1992; *Sandholt,* 1997; *Dunlop et al.,* 2000]. There are three major models describing the cusp morphology and dependence on external solar wind conditions, the MHD model, the turbulence/diffusive entry model, and the direct flowing entry model [see *Yamauchi and Lundin,* 2001 and references therein]. These models describe many of the special cusp properties, but they are differently successful in describing the low-resolution and high-resolution observations, so that none of them describes everything (see [*Yamauchi and Lundin,* 2001] for a full discussion).

The magnetospheric cusp plays an important role as the region of most direct connection between the ionosphere and the interplanetary medium through reconnection [*Smith and Lockwood,* 1996]. Reconnection between magnetospheric and interplanetary magnetic field lines is likely to occur whenever their directions (or at least one component) are anti-parallel [*Onsager and Fuselier,* 1994; *Fuselier et al.,* 1997]. During southward IMF condition, magnetic field lines in the subsolar region can connect to the solar wind magnetic field and become open. During northward IMF condition, reconnection can take place at the high latitude magnetopause. During intermediate conditions with small northward and dominating east-west component of the IMF, mixed situation with reconnection at the high- and the low-latitude region may occur simultaneously [*Reiff and Burch,* 1985].

Dayside auroral forms in the cusp region so far have mostly been classified from ground-based observations. During northward IMF conditions (clock angle $\theta < 45°$) bands of auroral emission dominate at high latitudes (78-79°, type 2 cusp aurora), during intermediate conditions ($\theta \approx 45 - 90°$) auroral bands are present at high and low ($< 75°$) latitudes, and during southward IMF ($\theta > 90°$) the high-latitude aurora disappears, and only the low-latitude forms (type 1 cusp aurora) remain [*Sandholt et al.,* 1998]. These auroral forms show asymmetries depending on the IMF east-west B_y component, and are related to reconnection processes at either high- or low magnetopause latitudes [*Øieroset et al.,* 1997].

In a recent paper, *Milan et al.* [2000] described an event study of an interval of northward IMF, where they observed luminosity near local noon poleward of the dayside auroral oval with the UVI instrument on the Polar satellite. They interpreted this emission as the signature of high latitude reconnection and described its motion in response to IMF B_y changes in coordination with observations of the large-scale convection flow by the CUTLASS Finland HF radar.

In this paper we are going to perform a statistical analysis of the correlation of intense proton aurora emission in the dayside cusp region as observed by the IMAGE-FUV instrument with the corresponding solar wind parameters. After a brief summary of instrumentation and analysis techniques we will discuss individual observations and finally summarize 18 cases in a statistical way.

2. Estimate of mean energy and energy flux in the cusp aurora

Auroral emissions can either be excited by precipitating electrons or protons [*Strickland et al.,* 1993]. Most emissions do not contain information about the identity of the exciting particle, as they originate from oxygen and nitrogen atoms, molecules, or ions of the upper atmosphere. Many previous papers on aurora observations interpreted all emissions as being caused by electron precipitation. However, energetic protons are very efficient in producing secondary electrons which in turn are capable of creating aurora indistinguishable from pure "electron aurora" [*Hubert et al.,* 2001]. Generally the flux of energetic protons is low and the contribution of protons to the aurora is small, but occasionally their contribution must be taken into account [*Frey et al.,* 2000].

The auroral emission in a particular region depends on the local precipitation characteristics (spectrum and flux) of electrons and protons and the composition of the atmosphere. A full model calculation of the expected auroral signal requires a full description of the particle spectrum for instance by measurements from a low altitude satellite as done in [*Frey et al.,* 2000]. This approach however, is impossible on a global scale because there are simply not enough satellites orbiting Earth. A global approach has to rely on certain simplifications and one reasonable way is the simplified description of the particle spectra by the mean energy and the total flux assuming a certain energy distribution function like Gaussian, Maxwellian, or kappa-functions. This approach requires the determination of only 5 unknown parameters, the atmospheric composition (O/N_2 ratio), the flux F and mean energies $< E >$ of precipitating electrons (e) and protons (p), respectively. The generalized simplified description of the signal in our instruments can then be given as

$$\begin{aligned} I(S12) &= F(p) * b_{s12}(<E_p>) \quad (1) \\ I(WIC) &= F(p) * b_{wic}(<E_p>) + F(e) * a_{wic}(<E_e>) \quad (2) \\ I(S13) &= F(p) * b_{s13}(<E_p>) + F(e) * a_{s13}(<E_e>) \quad (3) \end{aligned}$$

The measurements I(WIC), I(S12), and I(S13) provide three input parameters for solving the mathematical problem of simulating the global distribution of auroral emission. The parameters a and b with the subscripts for every instrument depend on the mean energy of the electrons and protons, and on instrument parameters like the width and location of the passband, the gain etc. For all our simulations we will assume a Maxwellian distribution for electrons and a kappa function for protons. Two of the unknown parameters (atmospheric composition and proton mean energy) will be eliminated in this approach. Here we use a single atmospheric composition altitude profile according to the MSIS model for high solar and moderate magnetic activity. The full description of this quantitative analysis of FUV-observations is beyond the scope of this paper and will be published elsewhere. Here we will use it to estimate the precipitation characteristics in the cusp.

3. Instrumentation and data analysis

The IMAGE satellite is in a highly elliptical orbit of 1000 x 45600 km altitude. The Far Ultra-Violet imager (FUV) consists of three imaging sub-instruments and observes the aurora for 5-10 seconds during every 2 minute spin period [*Mende et al.,* 2000]. The major properties like fields of view, spatial resolution and spectral sensitivity were validated by in-flight calibrations with stars [*Gladstone et al.,* 2001]. The Wideband Imaging Camera (WIC) has a passband of 140-180 nm. It measures emissions from the N_2 LBH-band and atomic NI lines, with small contributions from the OI 135.6 nm line. The proton aurora imaging Spectrographic Imager channel (SI-12) is sensitive to the Doppler-shifted Lyman-α emission around 121.8 nm from charge-exchanging precipitating protons. The instrument properties do not allow determination of the exact Doppler shift and the energy of the emitting hydrogen atom. However, as was confirmed by theoretical modeling, it is mostly sensitive to proton precipitation in the energy range of 2-8 keV, with very low sensitivity below 1 keV [*Gérard et al.,* 2000, 2001]. The oxygen imaging Spectrographic Imager channel (SI-13) has a passband of 5 nm around the 135.6 nm doublet of oxygen OI emission. The measured signal is a combination of OI and some contribution from lines in the N_2 LBH emission band (20-50 % depending on electron energy).

Solar wind parameters for this study were obtained through CDAWeb from the WIND and Geotail spacecraft. Geotail can be about 30 Earth radii in front of Earth but it also moves through the magnetosphere, when measurements were discarded for this study. Wind changed from a location 40 R_e in front of Earth to more than 200 R_e at the dawn side. All solar wind properties were propagated to Earth using the instantaneous solar wind speed values.

During the time period of June 5 to November 26, 2000 (days of year 157-331) 18 clear cases of a localized bright UV emission on the dayside were found (Table 1). Figure 1 shows examples from four different days, when the localized feature could be observed poleward of the dayside auroral oval location. These cases were especially pronounced in the images from the proton camera, because this channel does not suffer from a dayglow background. However, after proper dayglow subtraction, similar features could be seen in the other FUV channels as well (Figure 2). The two selection criteria for the events were:

Table 1

Figure 1

Figure 2

- A localized region of bright Doppler shifted Lyman alpha emission had to be found poleward of the dayside auroral oval.

- The localized region had to be observable for at least 30 minutes.

The second criterion removed several short time periods from the original selection (for instance 2000-268, 17:35-17:45 and 2000-315, 12:38-12:55). An image from another discarded time period (2000-160, 09:12-09:20) is given in [*Fuselier et al.,* 2001a]. Each individual time sequence was then analyzed in the SI-12 images in the following way. Whenever the bright feature was seen in the SI-12 images, the mean count rate in a region of 3x3 pixels (about 300x300 km from apogee) around the brightest pixel was determined, as well as the location in magnetic local time (MLT) and geomagnetic latitude. That location was then mapped into the images of SI-13 and WIC, where again the mean image intensity in an area of 3x3 or 5x5 pixels, respectively, was determined. If the localized emission vanished below background level, the last location was tracked for another 30 minutes. If the emission appeared again within 30 minutes, the whole sequence was considered as one event. If the emission did not appear again, 15 minutes after the disappearance were still included in this study.

4. FUV observations

4.1. Cusp aurora on November 8, 2000

FUV observations on November 8, 2000 (doy=313) show most clearly the relationship between the auroral emission from the cusp and the solar wind parameters (Figure 3). Over the course of 5 hours the solar wind dynamic pressure increased three times for short periods and the SI-12 signal closely followed these increases. The small differences in the arrival times of the shifted density pulses from Wind and Geotail are within the uncertainty range of 5 minutes. The IMF B_z component was almost steadily positive (northward) around 20 nT with short decreases during the times of pressure increases. All the other FUV instruments showed similar short increases in their output signal. How these changes are related to changes in the proton precipitation will be

Figure 3

discussed later.

4.2. Cusp aurora on September 17-18, 2000

Figure 4

The FUV observations on September 17-18, 2000 (doy=261-262) show the longest and clearest cusp signatures in this study. Figure 4 gives a summary of the observations between September 17, 17:48 UT and September 18, 15:53 UT. The signature of intense proton precipitation on the dayside appeared on September 17 after 16:00 UT and was observable until 19:53 UT, when the instrument was turned off before entering the radiation belt. When the FUV instrument turned on after leaving the radiation belt on September 18 at 01:28 UT an intense cusp signature could be observed and it remained strong until 10:13 UT when the instrument again was turned off before entering the radiation belt. See also Figure 2 for the signature in the other two FUV channels. At the beginning of the next orbit at 15:28 UT the same feature was there again, but this time it disappeared after 16:40 UT. There is good reason to believe, that the intense cusp proton precipitation disappeared after 13:00 UT and re-appeared shortly before instrument turn-on, and that it did not persist all the time when IMAGE was near perigee. The details of this will be discussed later.

Figure 5

The solar wind conditions are summarized in Figure 5. The solar wind density increased dramatically on September 17 around 16:00 UT (not shown) and remained high until 5:15 UT on September 18. The drop in density is followed by a decreasing signal in the proton imager (3rd panel). During this entire period the IMF remained strongly northward with a B_z always greater than 10 nT and as high as 29 nT. The B_y component changed from positive values before 01:30 UT to negative values later, and as a reaction the cusp signature changed location from 1330 MLT to 1030 MLT, which can also be seen in the second and third images in Figure 4. Later, the cusp location remained in the pre-noon region.

4.3. Cusp aurora on June 24, 2000

Figure 6

The observations on June 24, 2000 (doy=176) are summarized in Figure 6. The solar wind density had already increased before FUV turned on after leaving the radiation belt. The cusp signal decreased together with the density and it disappeared after 05:30, when B_z turned negative. A short-lived increase appeared at 06:25, when B_z turned northward again, but the signal remained very small, because the solar wind density was small, too. All data are shown in Figure 6 however, data after 05:45 were not included in this study as they failed to fulfill criterion 2 from section sec:instrument. There is some indication that the latitude location increased with decreasing solar wind density (around 0300-0400). A clear correspondence can again be seen between the MLT-location of the cusp signature and IMF B_y.

4.4. Cusp aurora on July 29, 2000

Figure 7

The observations on July 29, 2000 (doy=211) are summarized in Figure 7. The solar wind density had already increased before FUV turned on after leaving the radiation belt however, no cusp signal could be observed during the first 10 minutes of observation. It was only after 16:00 UT that the change of B_z to positive values caused a strong increase in the cusp signal. Later B_z remained very steady around 4 nT. The solar wind density increased after 17:30 UT, but the cusp signal decreased with time.

4.5. Cusp aurora on September 6, 2000

Figure 8

September 6, 2000 (doy=250) was a period of repeated disappearance and appearance of the localized emission and examples of proton observations are summarized in Figure 8. The solar wind density was high throughout the period and a cusp signature could be observed at 1500 MLT, due to the positive B_y component of 10 nT (solar wind data not shown). Suddenly, at 19:40 UT, B_z changed from 12 nT to -9 nT, and the cusp signature which could be seen around 1500 MLT and 80 degrees latitude disappeared. In response to this change, the dayside auroral oval got bright between 1100 and 1400 MLT and around 76 degrees latitude (third panel in Figure 8). The localized emission appeared again briefly 20:00, 20:20, 20:38-21:07. Later at 21:30 UT, B_z changed from -8 nT to 11 nT, and the cusp signature appeared again at 1200 MLT when IMF B_y was close to 0 nT. These observations with the appearance and disappearance of the high- and low-latitude cusp aurora are the same as described from ground-based observations by *Øieroset et al.* [1997].

5. Discussion

5.1. Location of cusp

All cusp observations were localized between 70.8° and 85.6° geomagnetic latitude. Figure 9 gives a summary of the locations in histogram format. The latitude distribution is slightly asymmetric with more samples above 78 degrees then below. The mean and median values are both 79.2°.

Figure 9

The location of the cusp in magnetic local time and latitude is shown in Figure 10. All locations are distributed along the dayside between 6.6 and 16.0 hours MLT, and the median and mean times have the same values of 11.7 hours.

Figure 10

5.2. Dependence of cusp characteristics on solar wind magnetic field

The propagated solar wind measurements were used to determine correlations between the proton precipitation location and intensity, and the solar wind magnetic field and plasma parameters. The relationship between the IMF GSM B_z value and the cusp location and Lyman alpha emission is given in Figure 11. Cusp observations were performed during B_z periods between -21 nT and 34 nT, but there does not seem to be a clear dependence of the latitude location and B_z. The intensity of the proton precipitation is strongly biased towards positive values of B_z. However, there is no clear correlation between both quantities, as the correlation coefficient reaches only 0.41.

Figure 11

There seem to be two subsets, one which contains small SI-12 signals for positive and negative values of B_z, and one which seems to show an increasing SI-12 signal with increasing positive B_z. However, both subsets could not very easily be separated.

Figure 12 summarizes the dependence of the cusp magnetic local time location and proton precipitation on the value of IMF B_y. There is a clear correlation between the location and B_y with pre-noon location for negative B_y and post-noon location for positive B_y. The least squares fit of all the data provided a result as

Figure 12

$$MLT = 11.8 + 0.127 B_y, \tag{4}$$

with B_y taken in nT, and MLT given in hours.

There is some indication that the response of the MLT location to IMF B_y changes is slower than for instance for emission changes in response to B_z changes (see for instance Figure 5). This finding is in agreement with [*Milan et al.,* 2000], who speculated about a dependence on the past history of the IMF.

5.3. Dependence of cusp characteristics on solar wind dynamic pressure

Figure 13 summarizes the dependence of the cusp proton precipitation on the solar wind dynamic pressure. A good correlation of 0.66 was obtained for the relation between the cusp signal and the dynamic pressure. The least squares fit result is

Figure 13

$$SI12 = 2 + 1.2 p_{dyn}, \tag{5}$$

with p_{dyn} in nPa, and SI12 given here as instrument counts. Assuming a mean energy of 2 keV for the precipitating protons, this would translate into a Lyman alpha intensity in Rayleighs of

$$I(Lyman_\alpha) = 500 + 300 p_{dyn}. \tag{6}$$

5.4. Summary of all correlations

The datasets were then used to determine any possible correlation between 13 parameters, like IMF components, solar wind density, pressure, velocity, and cusp signals and locations. A subset of the full 13x13 correlation matrix is given in equation 7.

$$
\begin{array}{lrrrrrr}
 & n & B_y & B_z & S12 & Lat. & LT \\
n & 1.00 & & & & & \\
B_y & 0.01 & 1.00 & & & & \\
B_z & -0.08 & -0.18 & 1.00 & & & \\
S12 & 0.31 & -0.13 & 0.41 & 1.00 & & \\
Lat. & -0.40 & -0.15 & 0.08 & -0.26 & 1.00 & \\
LT & -0.01 & 0.59 & -0.20 & -0.03 & -0.06 & 1.00 \\
p_{sw} & 0.75 & -0.16 & 0.25 & 0.65 & -0.27 & -0.14
\end{array}
\tag{7}
$$

The large correlation between the solar wind density n and the pressure p_{sw} is obvious as the pressure is calculated from the density. The matrix shows that the proton signal S12 correlates much better with pressure (0.65) then with density (0.31). Therefore, the solar wind bulk speed is an additional factor for an increased signal and not just the solar wind density. However, this could be caused by the fact that the proton imager SI-12 is insensitive to Doppler shifted Lyman alpha emission if the emitting hydrogen atom has less than 1 keV energy. The matrix also shows a reasonable correlation between the IMF B_y component and the MLT location of the cusp emission (0.59). The correlation between the IMF B_z and the proton signal is only 0.41, and reflects the fact that the cusp emission occurs with northward IMF, but its intensity is not related to the magnitude of B_z. There is some indication of an anti-correlation between the latitude location and the solar wind density and dynamic pressure, however the correlation coefficients of -0.40 and -0.27 do not allow for a definitive determination.

5.5. Mapping of cusp location into magnetosphere

Now that the characteristics of the cusp proton precipitation have been investigated, the next question is where the protons come from. A mapping code was developed which maps any location in an FUV-image into the magnetosphere [*Fuselier et al.,* 2001b]. It uses external solar wind parameters (IMF, pressure) and maps along the Tsyganenko magnetic field model [*Tsyganenko,* 1995; *Tsyganenko and Stern,* 1996]. Figures 14, 15, 16 show a representative example of this mapping for different locations in the proton camera image taken on September 18, 2000 at 02:46:29 UT. During this time period the IMF B_z had been strongly northward and almost stable for several hours and the time shifted value from the Wind spacecraft for this particular time was 23.3 nT (see Figure 5). The solar wind dynamic pressure was slowly decreasing, but still large at 20.2 nPa. These stable conditions allowed for a reliable use of IMF data, because even a propagation uncertainty of 5-10 minutes would not have changed the external parameters. Furthermore, the magnetosphere should have had enough time to reach relatively stable conditions without sudden external changes.

Figures 14, 1

Figure 14 contains three magnetic field lines originating at the poleward border of the cusp. Those field lines map into the lobe region of the magnetotail. During this particular time the cusp signature was not clearly separated from the dayside auroral oval, and therefore Figure 15 shows the mapping of field lines from a line between the equatorward border of the cusp and the poleward border of the dayside auroral oval. Those magnetic field lines map directly to the high latitude magnetopause. Finally, Figure 16 shows three mapped field lines from the equatorward border of the dayside auroral oval which map to the subsolar dayside magnetopause.

According to the model calculations the magnetopause was pushed inward to less than 8 R_e and it is very likely that pitch angle scattering in the subsolar magnetopause region is responsible for the intense proton precipitation into the dayside auroral oval region. The cusp signature, however, must have a different source. Under these northward IMF conditions direct magnetosheath precipitation after magnetic field reconnection in the high latitude lobe region is the most likely candidate.

5.6. Flux estimates

The quantitative analysis of flux estimates as outlined in section 2 starts with a kappa distribution of the protons with κ=3.5 [*Hubert et al.,* 2001] and an assumed mean proton energy in the cusp of 2 keV. This is a reasonable assumption according to statistical investigations of the average proton energy in the cusp [*Hardy et al.,* 1989, 1991].

The SI-12 signal in the cusp is used to determine the proton flux according to the left panel of Figure 17 and equation 1. The WIC and SI-13 signals are corrected for the proton produced contribution (Equations 2 and 3) and the ratio is then used to determine the mean energy of the precipitating electrons according to the right panel of Figure 17. This ratio is energy dependent because the SI-13 signal changes much more with energy of precipitating electrons then the WIC-signal, due to the deeper penetration of higher energy electrons into the atmosphere and the effect of UV-absorption by molecular oxygen. Therefore, the proton corrected WIC signal is finally used to determine the energy flux of electrons. The WIC/SI-13 ratio around 40 for most of the time in Figure 7 for instance indicates a low energy of precipitating electrons.

Figure 17

The results of flux estimates are given in Figure 18 where all 18 events are summarized and the simultaneous image sets are referred to as samples. The proton energy fluxes are, for most of the observations, between 0.05 and 1 mW/m^2 with a mean value of 0.5 mW/m^2, which are reasonable values compared to in-situ measurements by satellites like FAST or DMSP. After correcting for the proton contribution, the WIC/SI-13 ratio was used to calculate the mean energy of precipitating electrons, given in the next panel of Figure 18. Most of the time this energy is below 1 keV (mean value

Figure 18

910 eV), but there are several single data points with mean energies greater than 10 keV. Such mean energies are unreasonable for cusp precipitation. Here it has to be kept in mind, that the mean energy is estimated from the ratio of the WIC and SI-13 signals. Sometimes the SI-13 signal is very small (1-5 counts) on top of a dayglow signal of 20-40 counts. At such small count rates statistical fluctuations and a slightly incorrect dayglow subtraction may very easily change the ratio by 50 %. According to Figure 17, the WIC/SI-13 ratio is 60 for 1 keV electrons. A change of this ratio by 50 % gives 40 eV for a ratio of 30, and 3.8 keV for a ratio of 90.

The calculated electron energy fluxes (3rd panel Figure 18) are around 1 mW/m^2 for most of the observations, which again is a reasonable flux in the cusp. Large excursions from this value (samples 1200-1400), coincide with periods of very high solar wind dynamic pressure (4th panel). These deviations may indicate that the flux estimates may fail during periods of very large solar wind disturbances, when probably some of the simplifications outlined in Section 2 may not be justified.

Figure 19

Figure 19 summarizes the calculated ratio of proton energy flux to electron energy flux. Again a large fluctuation can be seen. However, here the uncertainty in the proton energy flux is not as large as the uncertainty in the electron energy flux because the SI-12 signal does not suffer from dayglow background. The median of the whole dataset is 0.26 and the mean is 0.30. This means that for this complete dataset, generally, protons carry 26-30 % of the energy flux that electrons do. This result is in very good agreement with a 27 % estimate from model calculations for cusp precipitation using the statistical distribution of electron and proton precipitation [*Hardy et al., 1985, 1989*] as input parameters [*Hubert et al.,* 2001].

The bottom panel of Figure 19 shows the ratio of the proton produced SI-13 signal to the total signal observed. The mean of this whole data set is 11 % but there are several cases where this ratio reaches 30 %. The implication of this result is that ground based observations of auroral emissions from the cusp may have overestimated the electron energy flux if the analysis assumed that all emission was produced by electrons. This could especially be the case for red-line observations at 6300 nm, because this emission is as unstructured as the proton precipitation and can be misinterpreted as the signature of soft electron precipitation.

Equation 5 relates SI-12 counts to the solar wind dynamic pressure. After crossing the bow shock, the solar wind is slowed down with a simultaneous increase in density and temperature [see e.g. *Walker and Russell,* 1995]. Therefore, the solar wind properties as measured by satellites will not be the same as properties for plasma entering the cusp. As a rough estimate however, we want to check if the solar wind in principle is able to provide the plasma, which could produce the cusp signature as seen by the proton imager.

From theoretical modeling we know that 36 SI-12 counts are produced by a flux of 1 mW/m^2 of 2 keV protons, which requires a particle flux of 3.1 10^{12} protons/m^2/s if we simply assume a monoenergetic beam. According to Equation 5 this requires a solar wind dynamic pressure of 28 nPa (see also Figure 13). During many of our events, a high solar wind density and bulk velocity produced such a high dynamic pressure. A 2 keV proton moves with a velocity of 619 km/s, which is not too high for many of our cases and will be used for the further calculations. The dynamic pressure of 28 nPa would then be produced by a density of 4.4 10^7 protons/m^3 (44 per cc), which move with an average speed of 619 km/s. Such a solar wind would provide a flux of 2.7 10^{13} protons, which is an order of magnitude more than would be required for the production of the proton aurora, if the solar wind could enter the cusp directly.

Previous observations by *Øieroset et al.,* [1997] showed particle data and discussed a proton acceleration by magnetic tension forces after high-latitude reconnection. Enhanced auroral green-light emission was explained by electron acceleration at the magnetopause or at lower altitude. In another study, enhanced ionization in the cusp proper could be explained by either 1 keV electron or 3 keV proton precipitation and was considered as a result of additional acceleration in the cusp [*Nilsson et al.,* 1998]. Here we show that the solar wind provides enough energy and particle flux for our observations. Even after the interaction of the solar wind with the bow shock and in the magnetosheath, the high energy tail of the Maxwellian solar wind proton distribution could account for our observations and an additional acceleration of the protons is not necessary to produce the observed cusp signatures in the optical emission from precipitating protons.

6. Conclusions

The major criterion for the case selection was a localized bright signal from proton precipitation poleward of the dayside auroral oval (Section 3). It turned out that this cusp signature is observable whenever the IMF is northward and the solar wind density is at least slightly increased. The intensity of the proton precipitation is then primarily controlled by the solar wind dynamic pressure. This result is in agreement with previous findings by *Newell and Meng* [1994], who also found a much stronger correlation of the cusp area with the solar wind dynamic pressure, than with the magnitude of $|B_z|$.

A change of the IMF B_z component to southward causes the localized cusp emission to disappear [*Fuselier et al.,* 2001b]. This is also the reason why we believe that the cusp signature disappeared during the perigee pass on September 18, 2000, when IMF B_z turned southward, and re-appeared shortly before the FUV observations with the northward turn of B_z as described in Section 4.2. The event summaries in Table 1 and Figure 11 show several sampling points with negative B_z. This represents the fact, that the original location of the cusp signature was tracked between repeated appearances and for 15 minutes more after it completely disappeared. A few of the B_z south points in Figure 11 may also be caused by the uncertainty in propagation time if the B_z suddenly turned southward. The mean values of B_z in Table 1 demonstrate the predominant occurrence during northward IMF.

The location of the cusp in local time is controlled by the IMF B_y component, with pre-noon locations for negative, and post-noon locations for positive B_y. The average location of all cases of this study was 79.1° geomagnetic latitude and 11.7 hours MLT. The brightest pixel method (see section 3) for the determination of the cusp location and the intensity of the Lyman Alpha signal was not always unique. At closer distances between the spacecraft and aurora, the cusp region extended over more than the 3x3 pixel area with many times more equally bright pixels. During weak UV emissions, the statistical fluctuations sometimes moved the brightest pixel around. However, with our large data set such fluctuations should have been averaged out. There is some indication that the response of the MLT location to IMF B_y changes is slower than for instance for emission changes in response to B_z changes. Other relations in this data set are not as obvious, though there are some indications of a correlation between latitude and solar wind dynamic pressure.

The cusp is known as a highly dynamic region and cusp crossings by satellites do not necessarily match with calculations of cusp locations [*Dunlop et al.,* 2000]. It can not be expected that a particular field line model will exactly determine the cusp location. Our results in Figures 14-16 should therefore be considered as general results rather than exact representations. The mapping indicated that the region of proton precipitation is magnetically connected to the high latitude magnetopause and the magnetospheric lobe region, and that high latitude reconnection is the most likely cause of this emission.

A case study by *Milan et al.* [2000] found a similar dependence of a localized emission on B_z and B_y. They attributed the observed luminosity to the precipitation of accelerated electrons. The three independent imaging channels of the FUV instrument enabled an estimate of the flux and energy of the precipitating protons and electrons. Though the whole process relies on certain assumptions and simplifications, the results were reasonable in comparison to particle measurements of other studies [see e.g. *Newell* *and Meng,* 1994; *Øieroset et al., 1997*]. These estimates confirm that under high solar wind dynamic pressure conditions protons can carry a significant amount of energy flux into the cusp, and that optical observations have to be corrected for this contribution, before electron precipitation characteristics can be determined.

Acknowledgments. We are grateful to the IMAGE-SMOC team who keep the spacecraft running. The IMAGE FUV investigation was supported by NASA through SwRI subcontract number 83820 at the University of California at Berkeley under contract number NAS5-96020. The solar wind measurements were obtained from CDAWeb. We acknowledge the following PIs: Wind Magnetic Fields Investigation: R. Lepping; Wind Solar Wind Experiment: K. Ogilvie; Geotail Magnetic Field Instrument: S. Kokubun; Geotail Comprehensive Plasma Instrument: L. Frank. J.C.G. is supported by the Belgian National Fund for Scientific Research (FNRS). His work was funded by the PRODEX program of the European Space Agency (ESA) and the Belgian Fund for Collective Fundamental Research (grant FRFC 97-2.4569.97).

References

Burch, J. L., Low-energy electron fluxes at latitudes above the auroral zone, *J. Geophys. Res., 73,* 3585, 1968.

Dunlop, M. W., P. J. Cargill, T. J. Stubbs, and P. Woolliams, The high-altitude cusps: HEOS2, *J. Geophys. Res., 105,* 27509, 2000.

Frank, L. A. and J. D. Craven, Imaging results from Dynamics Explorer 1, *Rev. Geophys., 2,* 249, 1988.

Frey, H. U., S. B. Mende, C. W. Carlson, J.-C. Gerard, B. Hubert, J. Spann, R. Gladstone, and T. J. Immel, The electron and proton aurora as seen by IMAGE-FUV and FAST, *Geophys. Res. Lett., 28,* 1135, 2001.

Fuselier, S. A., B. J. Anderson, and T. G. Onsager, Electron and ion signatures of field line topology at the low-shear magnetopause, *J. Geophys. Res., 102,* 4847, 1997.

Fuselier, S.A., A. G. Ghielmetti, T. E. Moore, M. R. Collier, J. M. Quinn, G. R. Wilson, P. Wurz, S. B. Mende, H. U. Frey, C. Jamar, J.-C. Gérard, J. L. Burch, Ion outflow observed by IMAGE: Implications for source regions and heating mechanisms, *Geophys. Res. Lett., 28,* 1163, 2001a.

Fuselier, S. A., H. U. Frey, K. J. Trattner, S. B. Mende, and J. L. Burch, Cusp aurora dependence on IMF B_z, submitted to *J. Geophys. Res.,* 2001b.

Gérard, J.-C., B. Hubert, D.V. Bisikalo, V.I. Shematovich, A model of the Lyman-α line profile in the proton aurora, *J. Geophys. Res., 105,* 15795, 2000.

Gérard, J.-C., B. Hubert, D.V. Bisikalo, V.I. Shematovich, H.U. Frey, S.B. Mende, M. Meurant, G.R. Gladstone and C.W. Carlson, Observation of the proton aurora with IMAGE-FUV and simultaneous ion flux in situ measurements, *J. Geophys. Res.,* in press, 2001.

Gladstone, G. R. et al., Stellar calibration of the WIC and SI imagers and the GEO photometers on IMAGE/FUV, *Poster presented at AGU Fall Meeting,* 2000.

Hardy, D. A., M. S. Gussenhoven, and E.Holeman, A statistical model of auroral electron precipitation, *J. Geophys. Res., 90,* 4229, 1985.

Hardy, D. A., M. S. Gussenhoven, and D. Brautigam, A statistical model of auroral ion precipitation, *J. Geophys. Res., 94,* 370, 1989.

Hardy, D. A., W. McNeil, M. S. Gussenhoven, and D. Brautigam, A statistical model of auroral ion precipitation, 2. Functional representation of the average patterns, *J. Geophys. Res., 96,* 5539, 1991.

Hubert, B., J.-C. Gérard, D. V. Bisikalo, V. I. Shematovich, and S. C. Solomon, The role of proton precipitation in the excitation of the auroral FUV emissions, in press *J. Geophys. Res.,* 2001.

Mende, S. B. et al., Far ultraviolet imaging from the IMAGE spacecraft, *Space Sci. Rev., 91,* 287, 2000.

Milan, S. E., M. Lester, S. W. H. Cowley, and M. Brittnacher, Dayside convection and auroral morphology during an interval of northward interplanetary magnetic field, *Ann. Geophys., 18,* 436-444, 2000.

Newell, P. T. and C.-I. Meng, Ionospheric projections of magnetospheric regions under low and high solar wind pressure conditions, *J. Geophys. Res., 99,* 273, 1994.

Nilsson, H., S. Kirkwood, and T. Moretto, Incoherent scatter radar observations of the cusp acceleration region and cusp field-aligned currents, *J. Geophys. Res., 103,* 26721, 1998.

Øieroset, M., P. E. Sandholt, W. F. Denig, S. W. H. Cowley, Northward interplanetary magnetic field cusp aurora and high-latitude magnetopause reconnection, *J. Geophys. Res., 102,* 11349, 1997.

Onsager, T. G. and S. A. Fuselier, The location of magnetic reconnection for northward and southward interplanetary magnetic field, in *Solar System Plasmas in Space and Time,* ed. by J. L. Burch and J. H. Waite, p. 183, AGU, Washington, D.C., 1994.

Reiff, P. H., T. W. Hill, and J. L. Burch, Solar wind plasma injection at the dayside magnetospheric cusp, *J. Geophys. Res., 82,* 479, 1977.

Reiff, P. H. and J. L. Burch, IMF B_y-dependent plasma flow and Birkeland currents in the dayside magnetosphere, 2. A global model for northward and southward IMF, *J. Geophys. Res., 90,* 1595, 1985.

Sandholt, P. E., Dayside polar cusp/cleft aurora: morphology and dynamics, *Phys. Chem.*

Earth, 22, 675, 1997.

Sandholt, P. E., C. J. Farrugia, J. Moen, O. Noraberg, B. Lybekk, T. Sten, and T. Hansen, A classification of dayside auroral forms and activities as a function of interplanetary magnetic field orientation, *J. Geophys. Res., 103,* 23325, 1998.

Smith, M. F. and M. Lockwood, Earth's magnetospheric cusps, *Rev. Geophys., 34,* 233, 1996.

Strickland, D. J., R. E. Daniell, J. R. Jasperse, and B. Basu, Transport-theoretic model for the electron-proton-hydrogen atom aurora, 2. Model results, *J. Geophys. Res., 98,* 21533, 1993.

Torr, M. R. et al., A far ultraviolet imager for the international solar-terrestrial physics mission, *Space Sci. Rev., 71,* 329, 1995.

Tsyganenko, N. A., Modeling the Earth's magnetospheric magnetic field confined within a realistic magnetopause, *J. Geophys. Res., 100,* 5599, 1995.

Tsyganenko, N. A. and D. P. Stern, A new-generation global magnetosphere field model, based on spacecraft magnetometer data, *ISTP Newsletter, 6,* 21, 1996.

Walker, R. J. and C. T. Russell, Solar-wind interactions with magnetized planets, in *Introduction to Space Physics,* edited by M. G. Kivelson and C. T. Russell, p. 178, Cambridge Univ. Press., Cambridge, 1995.

Woch, J. and R. Lundin, Magnetosheath plasma precipitation in the polar cusp and its control by the interplanetary magnetic field, *J. Geophys. Res., 97,* 1421, 1992.

Yamauchi, M. and R. Lundin, Comparison of various cusp models with high- and low-resolution observations, *Space Sci. Rev., 95,* 457, 2001.

H. U. Frey, S. B. Mende, T. J. Immel, Space Sciences Laboratory, University of California, Berkeley, CA 94720-7450 (e-mail: hfrey@ssl.berkeley.edu)

J. C. Gérard, B. Hubert, LPAP, Université de Liège, B-4000 Liège, Belgium (e-mail: gerard@astro.ulg.ac.be)

E.S. Claflin, S.A. Fuselier, Lockheed Martin ATC, 3251 Hanover St., Palo Alto, CA 94304-1191 (e-mail: stephen.a.fuselier@lmco.com)

Received ??? 2001; revised ??? 2001; accepted ??? 2001.

Figure 1. Examples of observations of the proton imager of FUV on four different days in 2000. The original images were re-mapped into a MLT-latitude grid with local noon at the top, midnight at the bottom, and dawn to the right of each image. At some times the spacecraft was too close to the Earth to image the whole auroral oval.

Figure 2. Observation of all three FUV instruments on September 18, 2000 at 04:02:01. The format of each image is the same as in Figure 1. The proton image is on the left, the oxygen image in the middle, and the wide-band image on the right.

Figure 3. Summary of ultraviolet observations from the cusp and related solar wind parameters for November 8, 2000 (doy=313). The panels from top to bottom show the time shifted solar wind proton density (Wind solid line, Geotail dashed line), the Wind-measured IMF-GSM B_z (solid line) and B_y (dashed line) components, the brightest proton aurora emission (instrument counts), the emission in the wide-band imaging camera (instrument counts) and the oxygen imager (instrument counts) in the corresponding regions.

Figure 4. Examples of observations by the FUV proton imager on September 17 and 18, 2000. The format is the same as in Figure 1.

Figure 5. Summary of ultraviolet observations from the cusp and related solar wind parameters for September 18, 2000. The top panel shows the time shifted solar wind proton density measured by Wind. The next panel gives the time shifted IMF-GSM B_z (solid line) and B_y (dashed line) components. The following panels show the proton imager signal in the cusp (instrument counts), and the latitude and MLT location of the cusp.

Figure 6. Summary of ultraviolet observations from the cusp and related solar wind parameters for June 24, 2000. The top panel shows the time shifted solar wind proton density measured by Wind (solid) and Geotail (dashed line). The next panel gives the time shifted IMF-GSM B_z (solid line) and B_y (dashed line) components. The following panels show the proton imager signal in the cusp (instrument counts), and the latitude and MLT location of the cusp.

Figure 7. Summary of ultraviolet observations from the cusp and related solar wind parameters for July 29, 2000. The top panel shows the time shifted solar wind proton density measured by Wind. The next panel gives the time shifted IMF-GSM B_z (solid line) and B_y (dashed line) components. The following panels show the proton imager signal in the cusp (instrument counts), and the WIC/SI-13 signal ratio at the corresponding location.

Figure 8. Examples of observations of the FUV proton imager on September 6, 2000. The format is the same as in Figure 1.

Figure 9. Histogram of the distribution of cusp observations in geomagnetic latitude.

Figure 10. Distribution of cusp observations in magnetic local time and geomagnetic latitude. The mean and median values are similar with 79.1° latitude and 11.7 hours magnetic local time.

Figure 11. Dependence of the cusp latitude location and cusp proton precipitation on the value of the IMF B_z.

Figure 12. Dependence of the cusp local time location and cusp proton precipitation on the value of IMF B_y. The top panel also shows the least square fitted linear relation of $\mathrm{MLT}=11.8 + 0.127B_y$.

Figure 13. Dependence of the cusp latitude location and cusp proton precipitation on the solar wind dynamic pressure. The top panel also shows the least square fitted linear relation of $\mathrm{SI12} = 2 + 1.2\ p_{dyn}$.

Figure 14. Result of field line mapping from the auroral region into the magnetosphere. The bottom middle panel shows the original image taken by the proton camera at 02:46:29 on September 18, 2000. Three points along the poleward border of the cusp signature were selected and magnetic fields lines from those locations were mapped into the magnetosphere. The three top panels show these field lines looking from dusk, from the sun, and from above the north pole, respectively. The bottom left panel shows these field lines in the rotated plane.

Figure 15. The same as Figure 14 but for three magnetic field lines passing through points along the line between the equatorward region of the cusp signature and the poleward border of the dayside auroral oval.

Figure 16. The same as Figure 14 but for three magnetic field lines passing through points along the equatorward border of the dayside auroral oval.

Figure 17. Dependence of the SI-12 signal on the mean proton energy for a unit flux of 1 mW/m^2 (left). The right panel gives the energy dependence of the ratio between the WIC and SI-13 signal for a pure proton or electron produced UV emission.

Figure 18. Result of flux estimates for all 18 events where all 2030 image sets are considered as individual samples. The left panel shows the proton energy flux calculated from the SI-12 signal assuming 2 keV proton precipitation. The next panel shows the mean electron energy after correcting the WIC and SI-13 signals for the proton contribution. The next panel shows the estimated electron energy flux, if the SI-13 signal is analyzed using the mean electron energy from the previous panel. The panel to the right shows the time shifted solar wind dynamic pressure for the respective times of image sets.

Figure 19. Ratio between the estimated energy flux carries by protons and that carried by electrons into the cusp (top). The bottom panel shows how much of the total SI-13 signal was produced by precipitating protons.

Table 1. Summary of all events used for this study. The time intervals are given in UT of FUV observations. The solar wind values are shifted for the propagation time. Density values show the range in cm^{-3}. The magnetic field values show the range for the full time interval and the mean value, rounded to the nearest integer.

Date and Time	Density	B_y	B_z
2000-176, 01:54-05:45	6-42	-12 to +10 (-4)	-6 to +14 (+4)
2000-178, 11:10-12:12	2-18	-16 to -3 (-9)	-10 to +33 (+1)
2000-183, 19:13-20:39	9-15	-3 to 0 (-2)	+4 to +4 (+5)
2000-195, 15:24-19:28	6-12	-2 to +11 (+5)	-1 to +10 (+4)
2000-210, 11:14-14:06	11-40	0 to +21 (+15)	-17 to +19 (+1)
2000-211, 15:46-19:02	10-21	-2 to +4 (+2)	-2 to +5 (+4)
2000-218, 04:35-09:55	1-12	-7 to +10 (+4)	-20 to +20 (+2)
2000-240, 17:01-21:22	6-17	-6 to +4 (-1)	-5 to +3 (+1)
2000-250, 18:46-22:41	3-26	-4 to +15 (+6)	-12 to +13 (+4)
2000-261, 15:01-19:33	5-27	-27 to +13 (-5)	-20 to +33 (+15)
2000-262, 01:29-09:43	2-35	-16 to +2 (-9)	+12 to +29 (+19)
2000-262, 15:28-18:42	2-23	-11 to +4 (-5)	-8 to +11 (+3)
2000-263, 06:13-09:51	1-12	-9 to +4 (-3)	-2 to +9 (+5)
2000-279, 06:20-11:10	14-74	-19 to +24 (0)	-26 to +21 (+7)
2000-309, 02:02-04:18	12-51	-22 to 0 (-12)	-9 to +15 (+2)
2000-311, 21:49-23:02	1-29	-1 to +9 (+5)	-13 to +9 (+1)
2000-313, 02:33-08:19	2-53	-10 to +10 (-1)	+3 to +18 (+15)
2000-331, 11:16-18:45	6-36	-14 to +16 (+2)	-14 to +19 (+9)

Figure 1

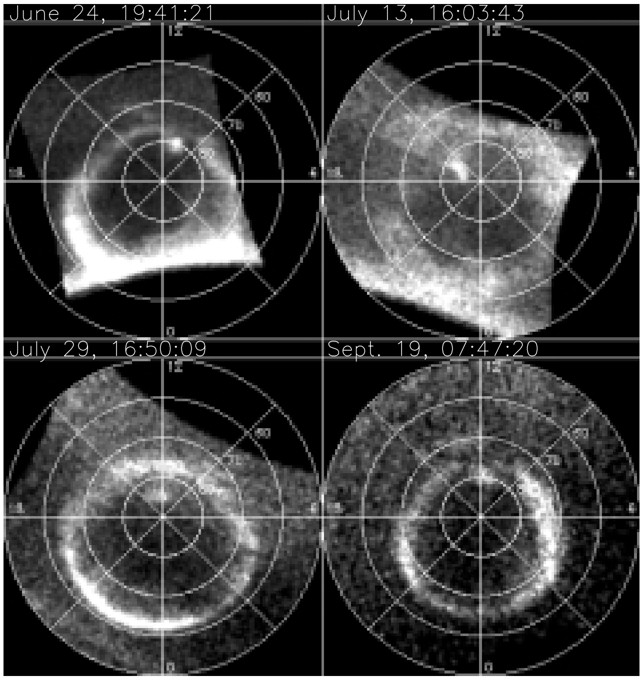

Thu Jun 21 16:15:09 2001 hfrey
/disks/sprite/disk1/hfrey/idl/image/fuview/show_cusp_examples

Figure 2

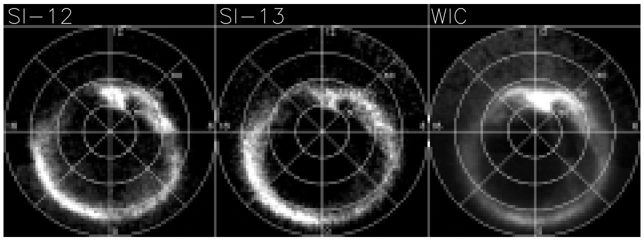

Thu Jun 21 16:22:23 2001, hfrey
/disks/sprite/disk1/hfrey/idl/image/fuview/show_cusp_examples

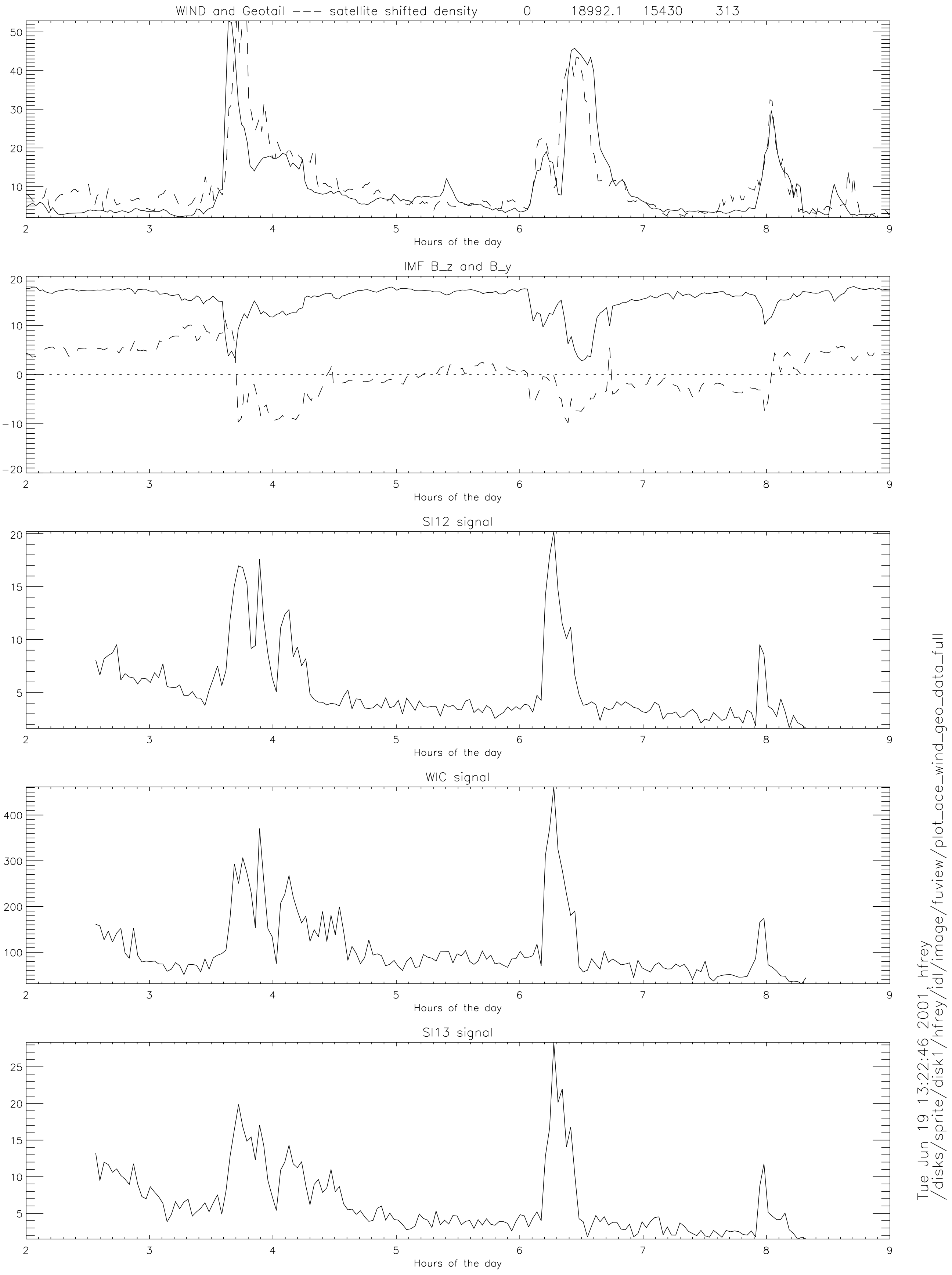
WIND and Geotail --- satellite shifted density 0 18992.1 15430 313
50
40
30
20
10
IMF B_z and B_y
20
10
0
−10
−20
SI12 signal
20
15
10
5
WIC signal
400
300
200
100
SI13 signal
25
20
15
10
5
2
3
4
5
6
7
8
9
Hours of the day
Tue Jun 19 13:22:46 2001, hfrey
/disks/sprite/disk1/hfrey/idl/image/fuview/plot_ace_wind_geo_data_full

Figure 3

Figure 4

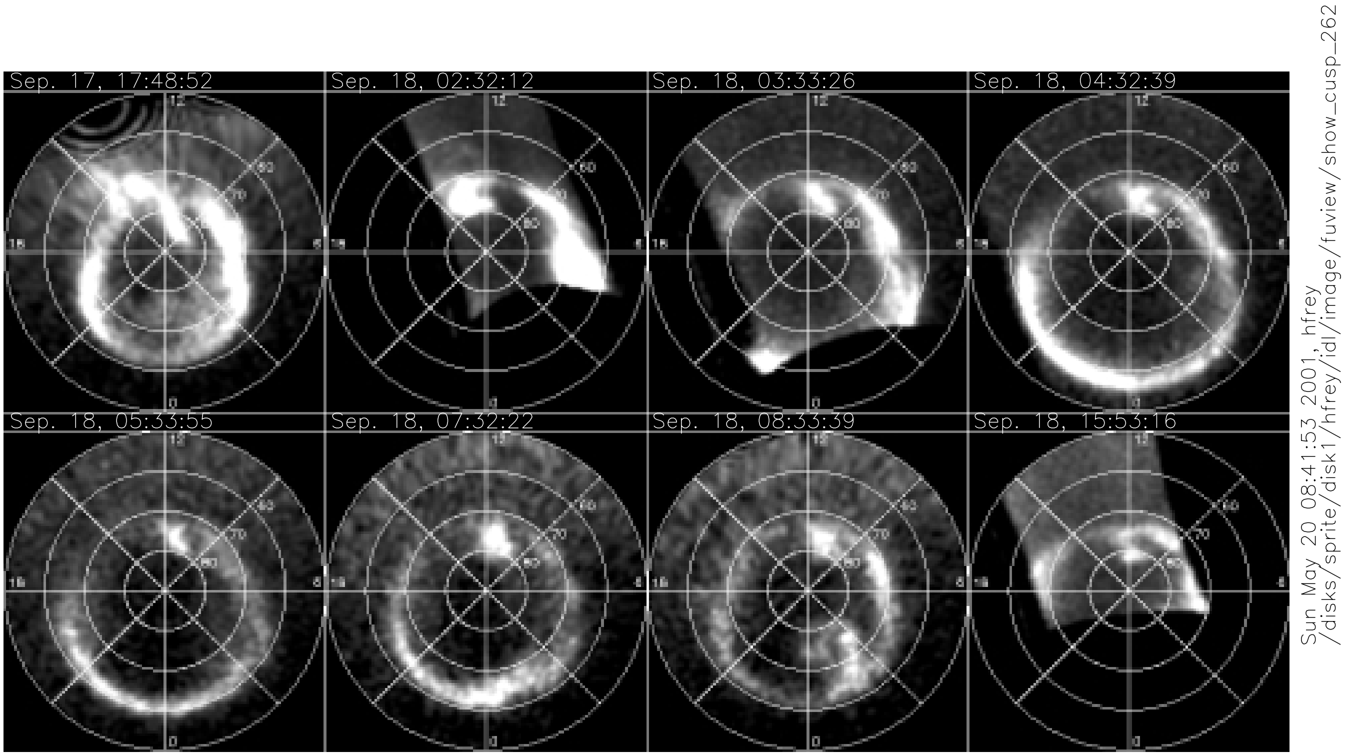
Sep. 17, 17:48:52
Sep. 18, 02:32:12
Sep. 18, 03:33:26
Sep. 18, 04:32:39
Sep. 18, 05:33:55
Sep. 18, 07:32:22
Sep. 18, 08:33:39
Sep. 18, 15:53:16
12
18
6
0
60
70
80
Sun May 20 08:41:53 2001, hfrey
/disks/sprite/disk1/hfrey/idl/image/fuview/show_cusp_262

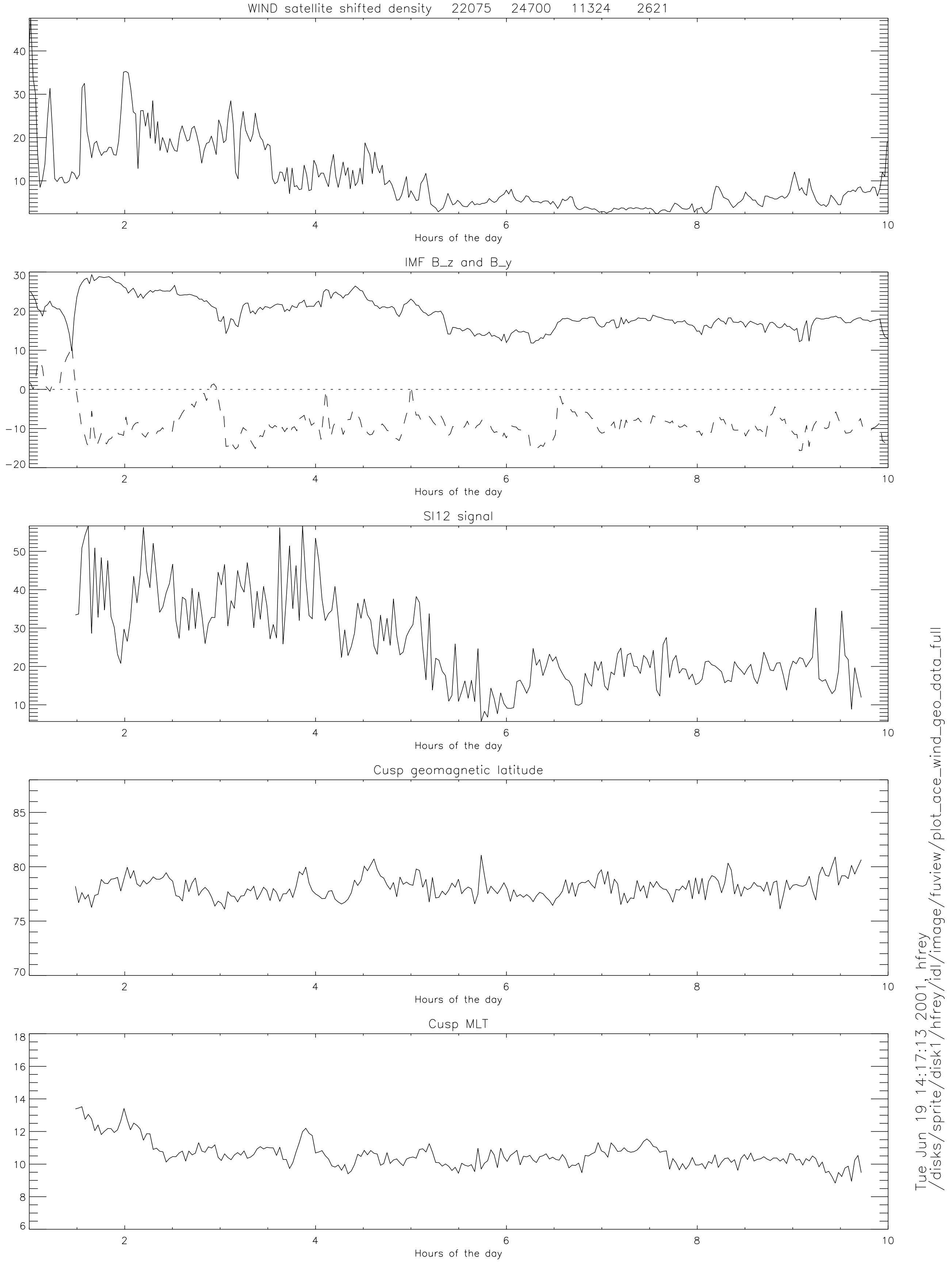
WIND satellite shifted density 22075 24700 11324 2621
40
30
20
10
2
4
6
8
10
Hours of the day
IMF B_z and B_y
30
20
10
0
−10
−20
2
4
6
8
10
Hours of the day
SI12 signal
50
40
30
20
10
2
4
6
8
10
Hours of the day
Cusp geomagnetic latitude
85
80
75
70
2
4
6
8
10
Hours of the day
Cusp MLT
18
16
14
12
10
8
6
2
4
6
8
10
Hours of the day
Tue Jun 19 14:17:13 2001, hfrey
/disks/sprite/disk1/hfrey/idl/image/fuview/plot_ace_wind_geo_data_full

Figure 5

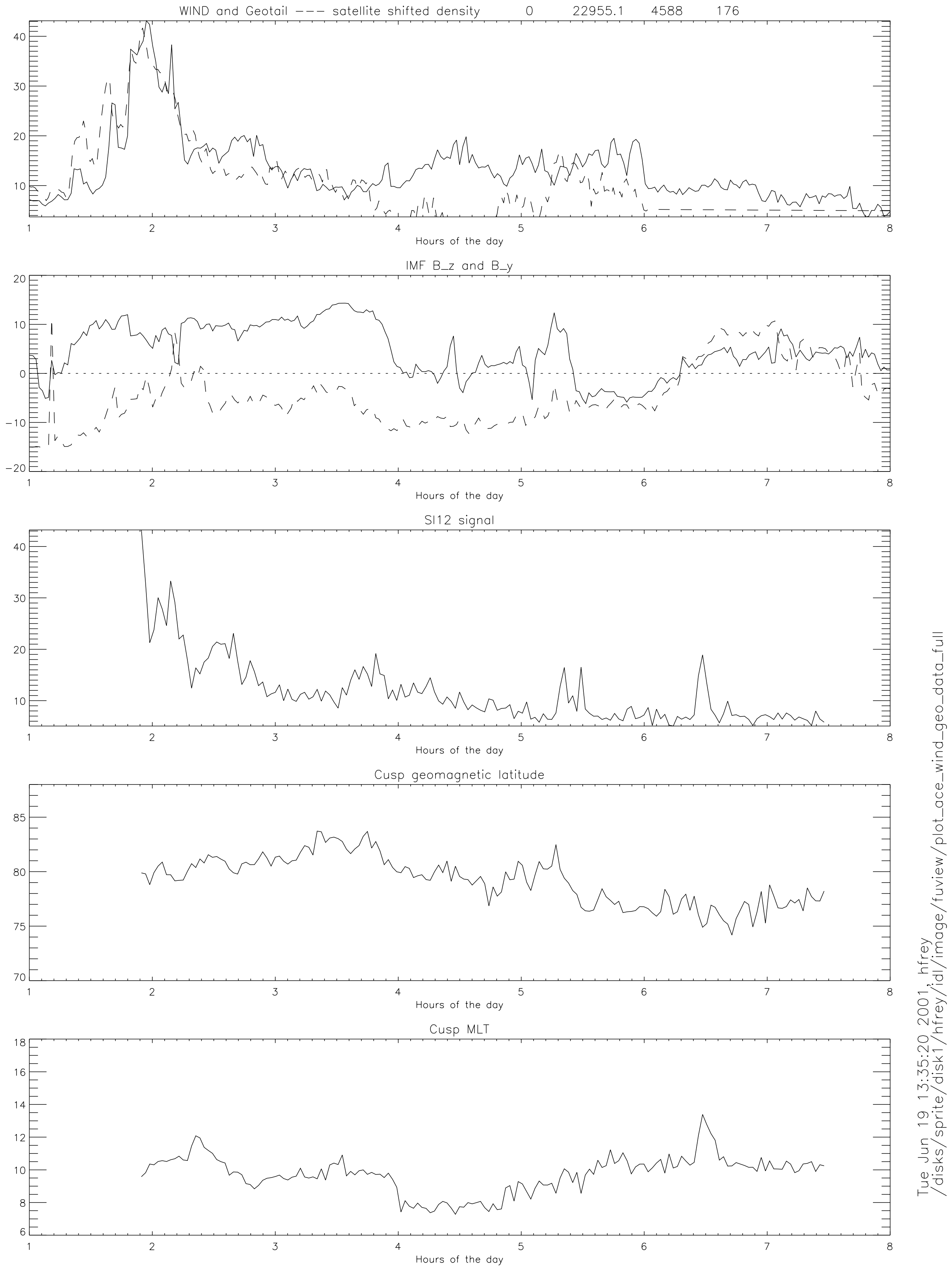
WIND and Geotail --- satellite shifted density 0 22955.1 4588 176
40
30
20
10
1
2
3
4
5
6
7
8
Hours of the day
IMF B_z and B_y
20
10
0
−10
−20
Hours of the day
SI12 signal
40
30
20
10
Hours of the day
Cusp geomagnetic latitude
85
80
75
70
Hours of the day
Cusp MLT
18
16
14
12
10
8
6
Hours of the day
Tue Jun 19 13:35:20 2001, hfrey
/disks/sprite/disk1/hfrey/idl/image/fuview/plot_ace_wind_geo_data_full

Figure 6

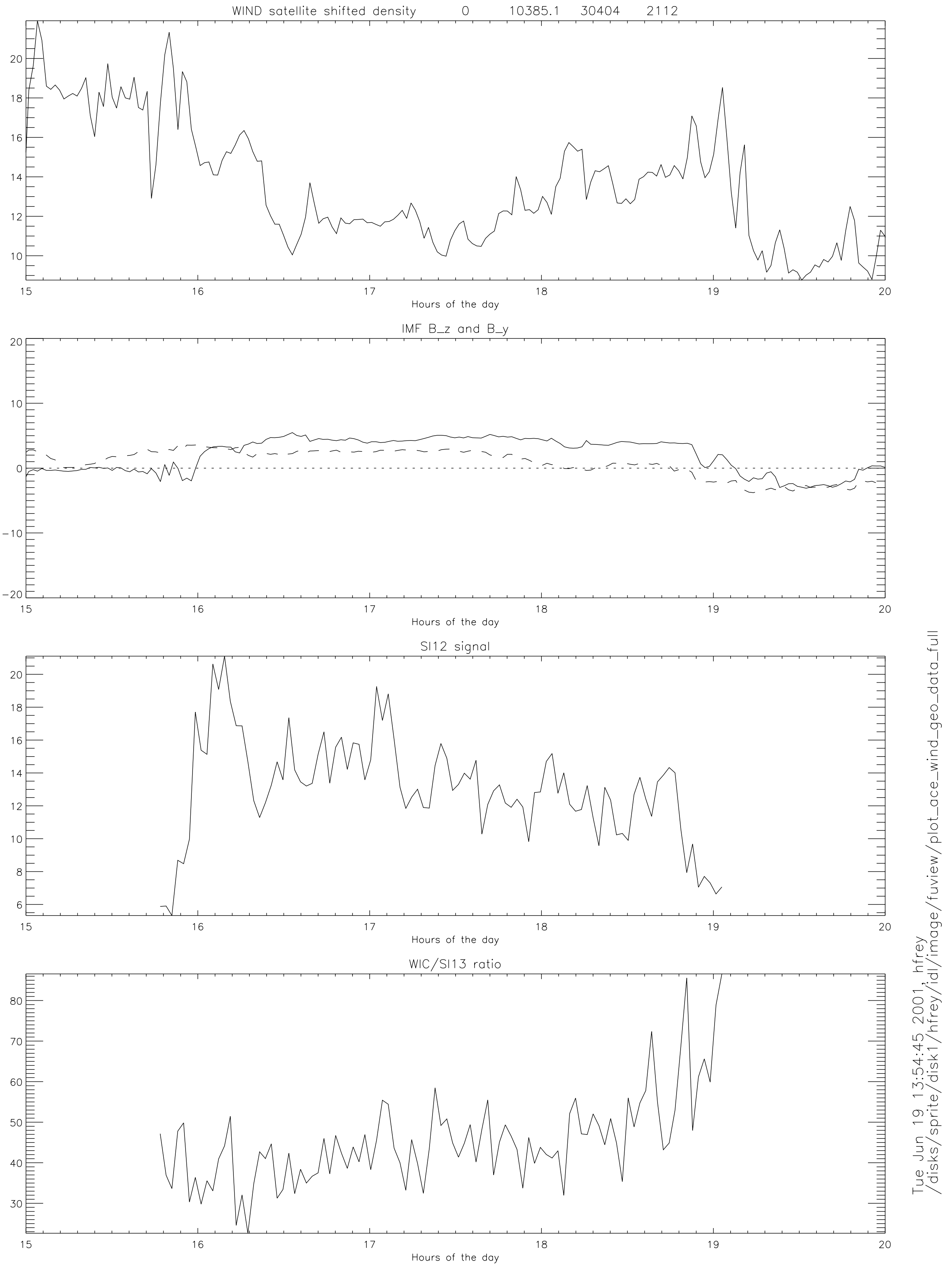
WIND satellite shifted density 0 10385.1 30404 2112
20
18
16
14
12
10
15
16
17
18
19
20
Hours of the day
IMF B_z and B_y
20
10
0
−10
−20
15
16
17
18
19
20
Hours of the day
SI12 signal
20
18
16
14
12
10
8
6
15
16
17
18
19
20
Hours of the day
WIC/SI13 ratio
80
70
60
50
40
30
15
16
17
18
19
20
Hours of the day
Tue Jun 19 13:54:45 2001, hfrey
/disks/sprite/disk1/hfrey/idl/image/fuview/plot_ace_wind_geo_data_full

Figure 7

Figure 8

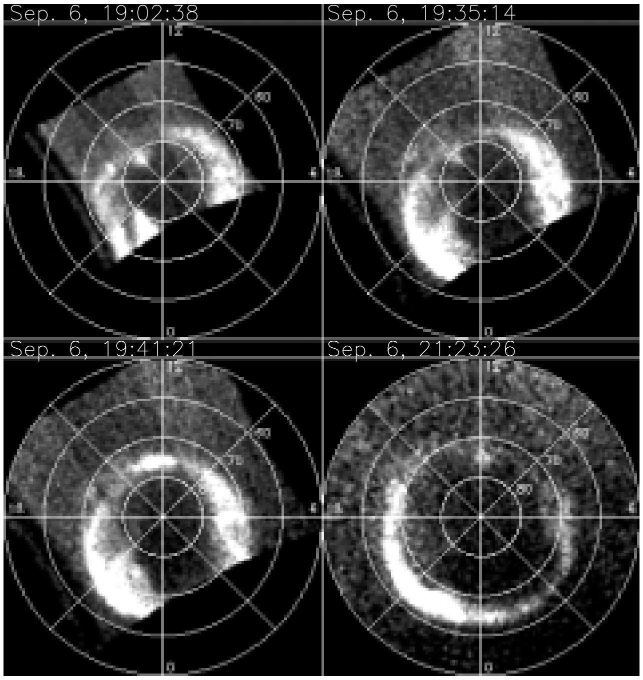
Sep. 6, 19:02:38
Sep. 6, 19:35:14
Sep. 6, 19:41:21
Sep. 6, 21:23:26
12
18
6
0
80
70
60
Tue Jun 19 16:55:11 2001, hfrey
/disks/sprite/disk1/hfrey/idl/image/fuview/show_cusp_250

Figure 9

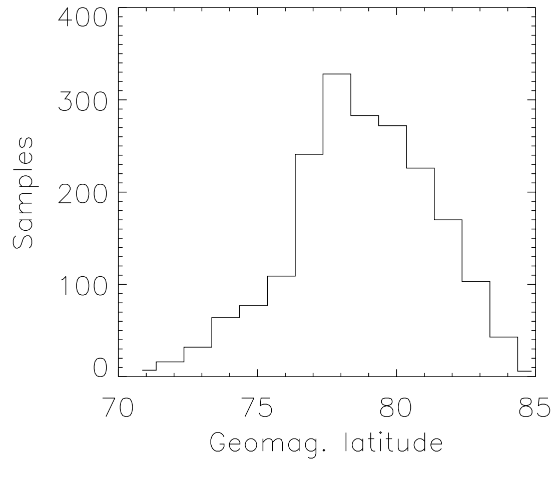

Fri Aug 31 14:46:35 2001, hfrey
/disks/sprite/disk1/hfrey/idl/image/fuview/mach_all_cusp_figures_newest

Figure 10

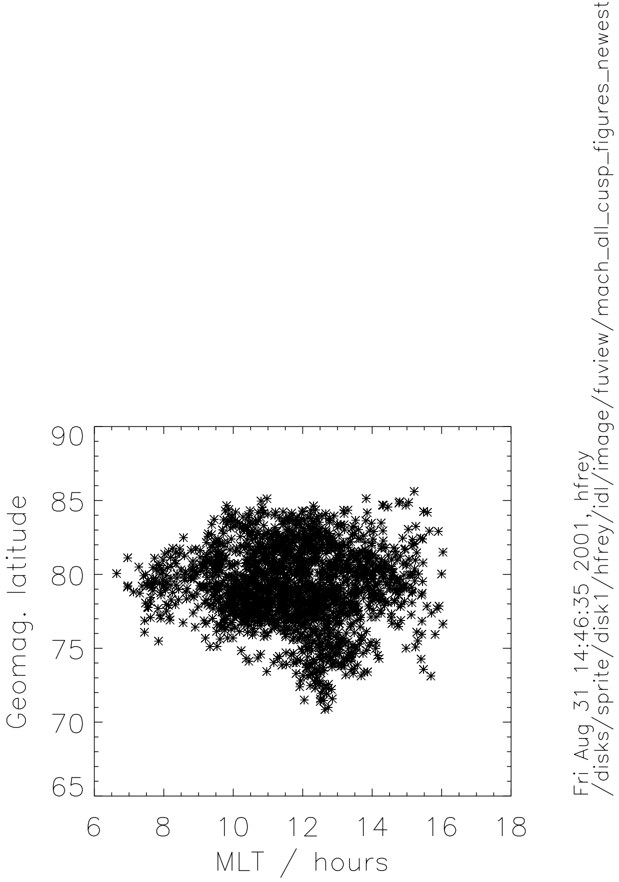
Geomag. latitude
90
85
80
75
70
65
6
8
10
12
14
16
18
MLT / hours
Fri Aug 31 14:46:35 2001, hfrey
/disks/sprite/disk1/hfrey/idl/image/fuview/mach_all_cusp_figures_newest

Figure 11

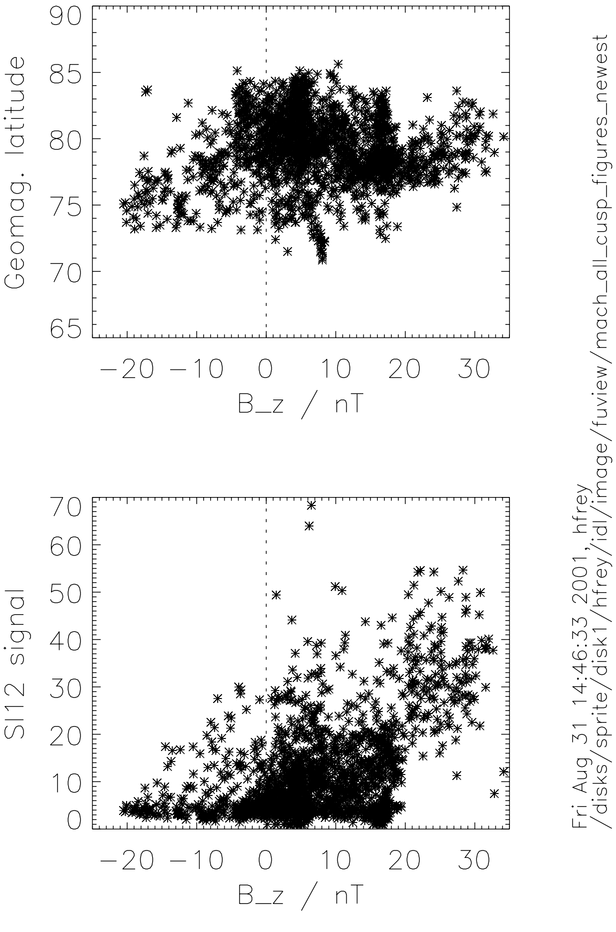
Geomag. latitude
90
85
80
75
70
65
−20
−10
0
10
20
30
B_z / nT
SI12 signal
70
60
50
40
30
20
10
0
−20
−10
0
10
20
30
B_z / nT
Fri Aug 31 14:46:33 2001, hfrey
/disks/sprite/disk1/hfrey/idl/image/fuview/mach_all_cusp_figures_newest

Figure 12

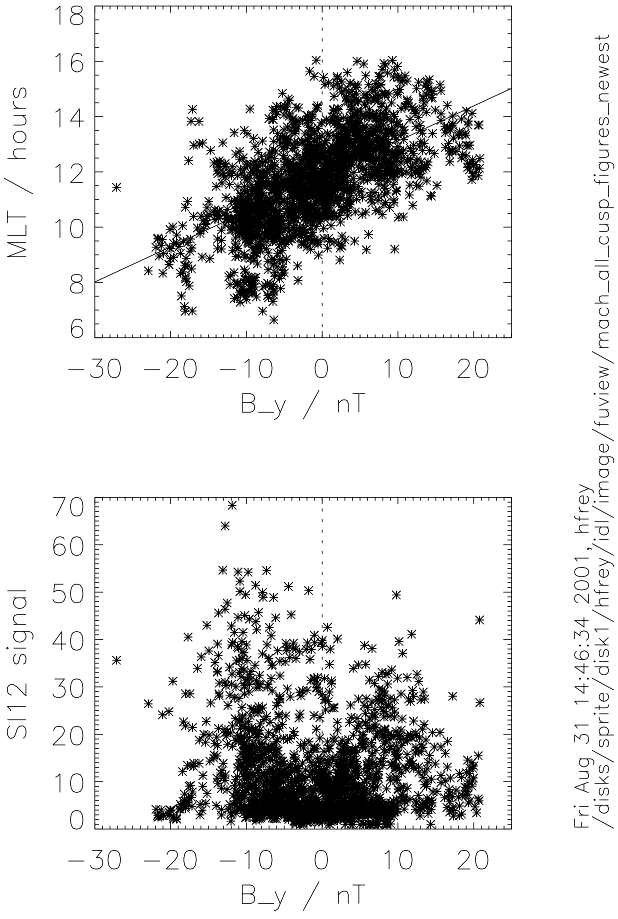
MLT / hours
18
16
14
12
10
8
6
−30
−20
−10
0
10
20
B_y / nT
SI12 signal
70
60
50
40
30
20
10
0
−30
−20
−10
0
10
20
B_y / nT
Fri Aug 31 14:46:34 2001, hfrey
/disks/sprite/disk1/hfrey/idl/image/fuview/mach_all_cusp_figures_newest

Figure 13

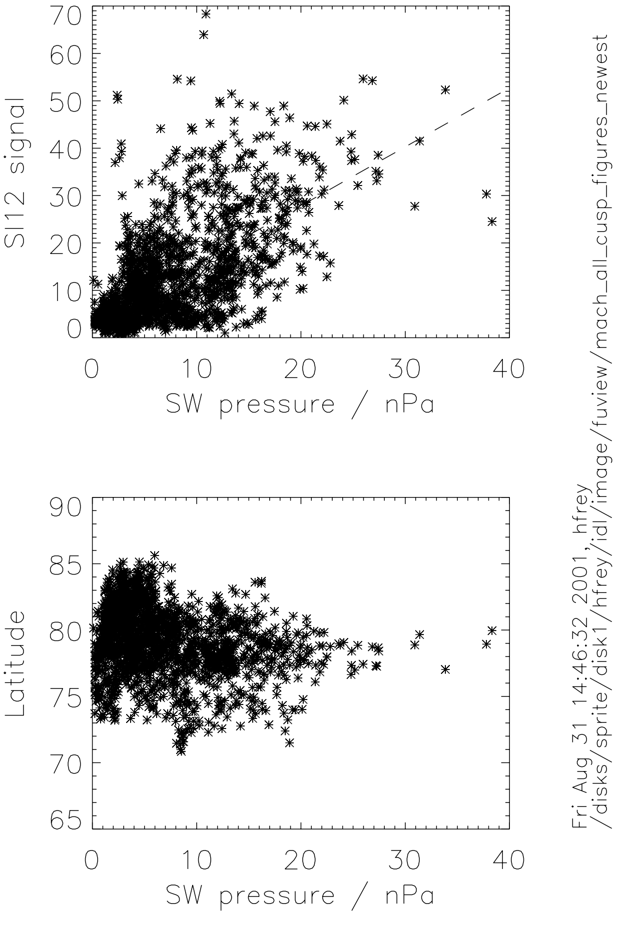

SI12 signal
70
60
50
40
30
20
10
0
0
10
20
30
40
SW pressure / nPa
Latitude
90
85
80
75
70
65
0
10
20
30
40
SW pressure / nPa
Fri Aug 31 14:46:32 2001, hfrey
/disks/sprite/disk1/hfrey/idl/image/fuview/mach_all_cusp_figures_newest

IMAGE/S12
18-Sep-2000 (00262)   Time: 02 46 29
Tilt Angle: -7.4 deg
Dst: -147 nT

WIND
Time: 02 43 00.5   Delay: 3.0 min
DynP: 20.2 nPa   Bswx: 15.2 nT
Bswy: -2.1 nT   Bswz: 23.3 nT

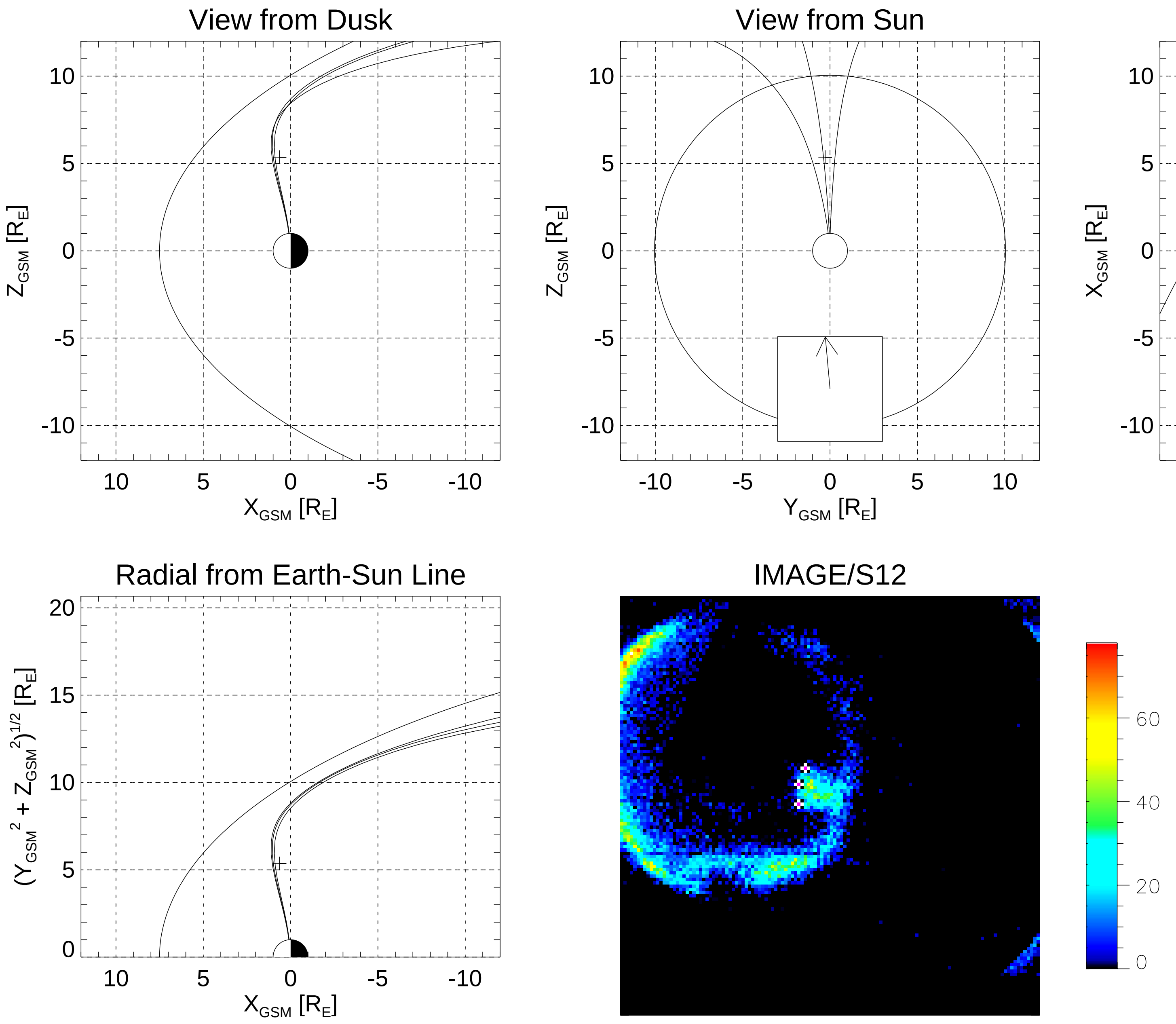

Lat, N	Lon, E	Indices
83.54	197.05	(113,151)
86.05	175.87	(109,141)
85.78	125.05	(109,129)

Ver. 1.6
28-Jun-2001

Figure 14

IMAGE/S12
18-Sep-2000 (00262)   Time: 02 46 29
Tilt Angle: -7.4 deg
Dst: -147 nT

WIND
Time: 02 43 00.5   Delay: 3.0 min
DynP: 20.2 nPa   Bswx: 15.2 nT
Bswy: -2.1 nT   Bswz: 23.3 nT

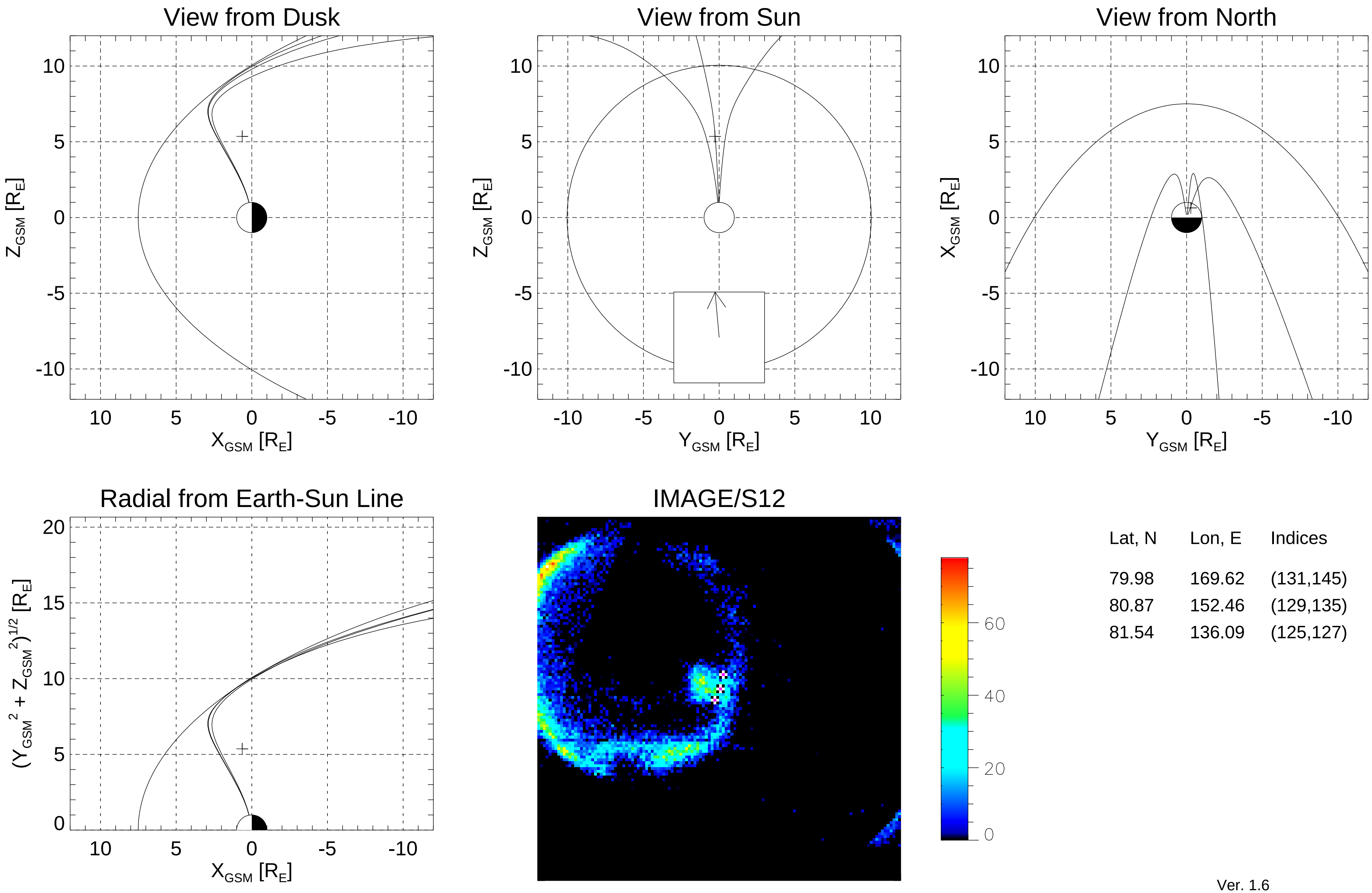

Lat, N	Lon, E	Indices
79.98	169.62	(131,145)
80.87	152.46	(129,135)
81.54	136.09	(125,127)

Ver. 1.6
28-Jun-2001

Figure 15

IMAGE/S12
18-Sep-2000 (00262) Time: 02 46 29
Tilt Angle: -7.4 deg
Dst: -147 nT

WIND
Time: 02 43 00.5 Delay: 3.0 min
DynP: 20.2 nPa Bswx: 15.2 nT
Bswy: -2.1 nT Bswz: 23.3 nT

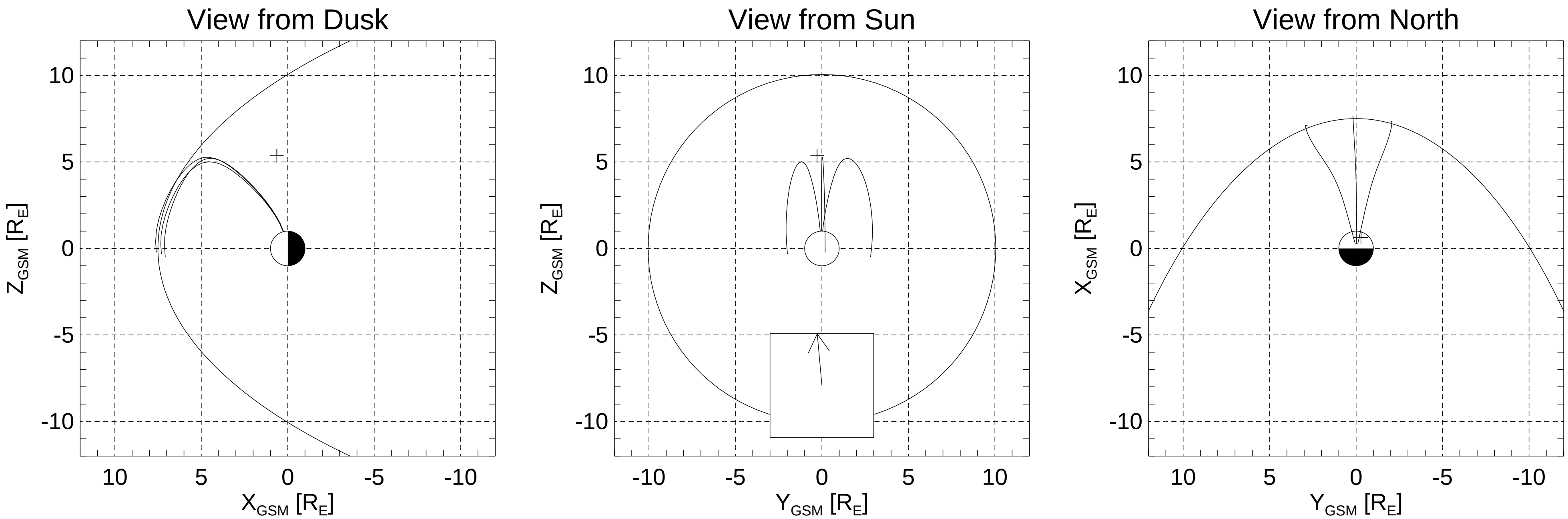

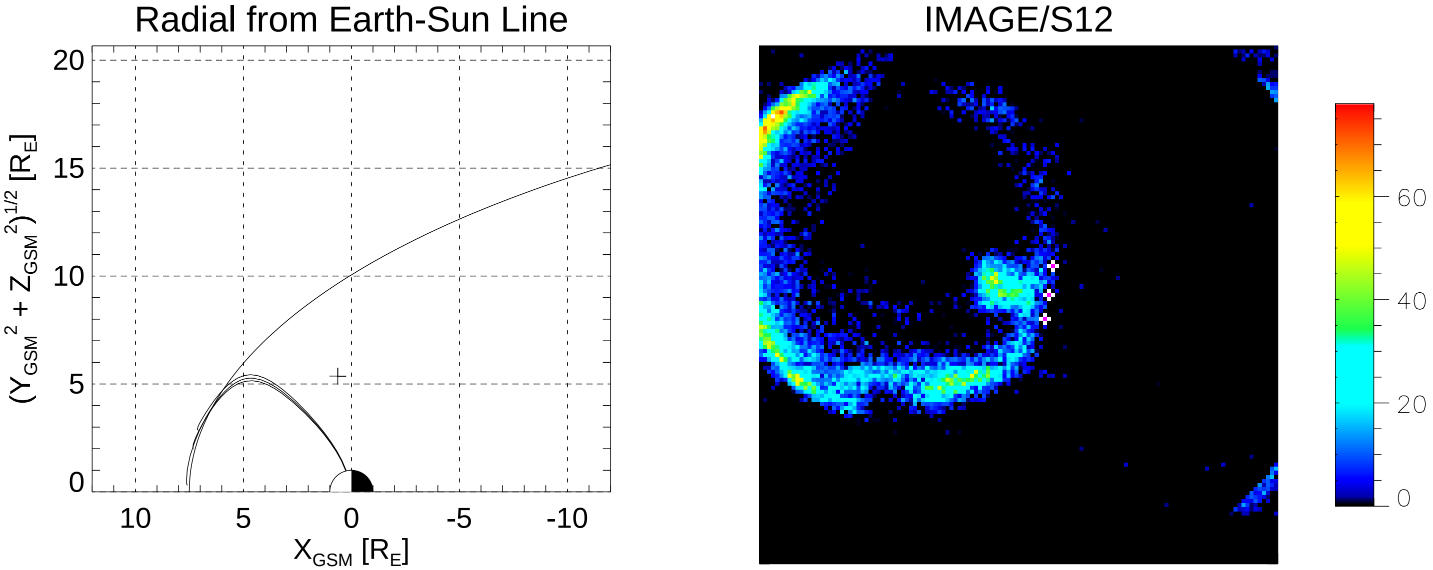

Lat, N	Lon, E	Indices
76.09	167.86	(145,147)
76.99	150.42	(143,133)
76.79	134.68	(141,121)

Ver. 1.6
28-Jun-2001

Figure 16

Figure 17

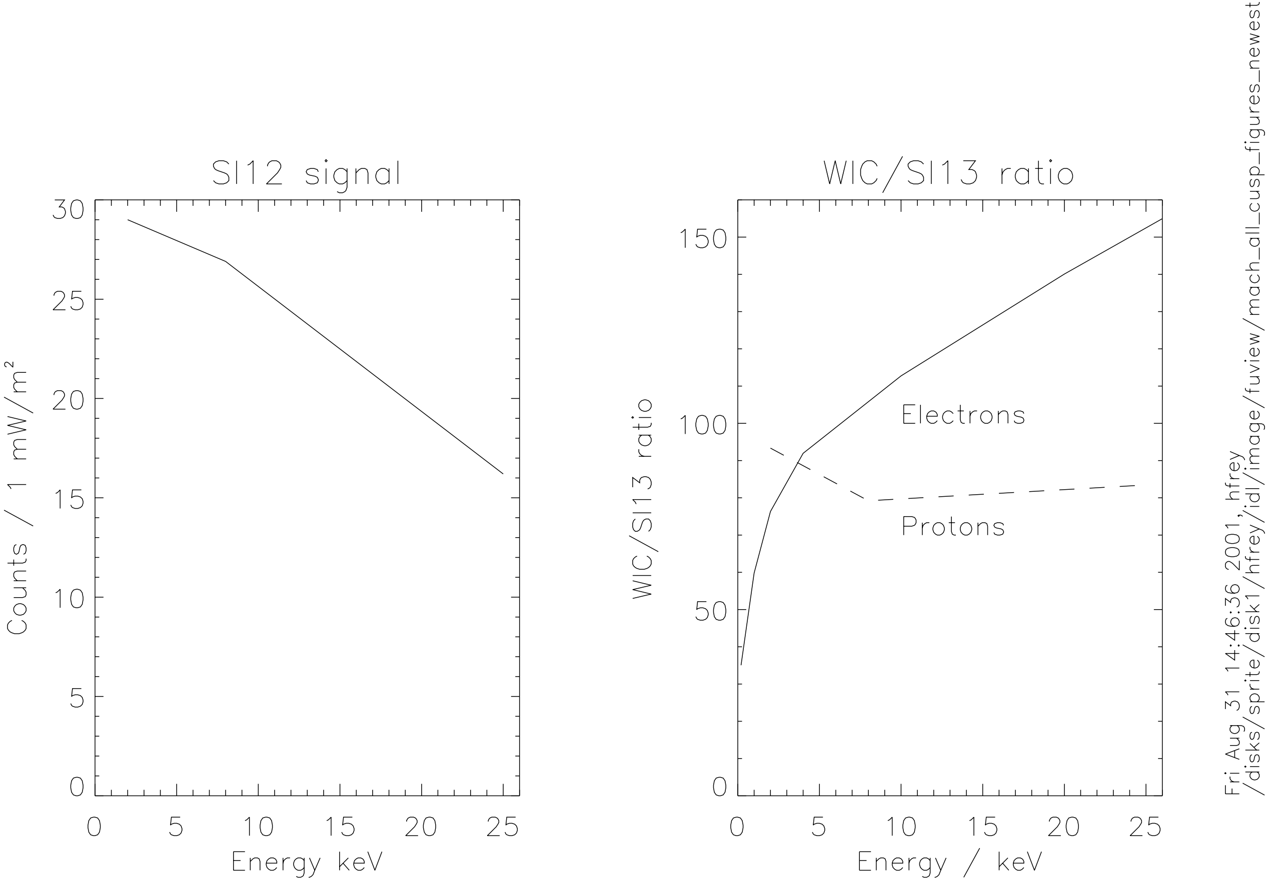
SI12 signal
Counts / 1 mW/m²
30
25
20
15
10
5
0
0
5
10
15
20
25
Energy keV
WIC/SI13 ratio
WIC/SI13 ratio
150
100
50
0
0
5
10
15
20
25
Energy / keV
Electrons
Protons
Fri Aug 31 14:46:36 2001, hfrey
/disks/sprite/disk1/hfrey/idl/image/fuview/mach_all_cusp_figures_newest

Figure 18

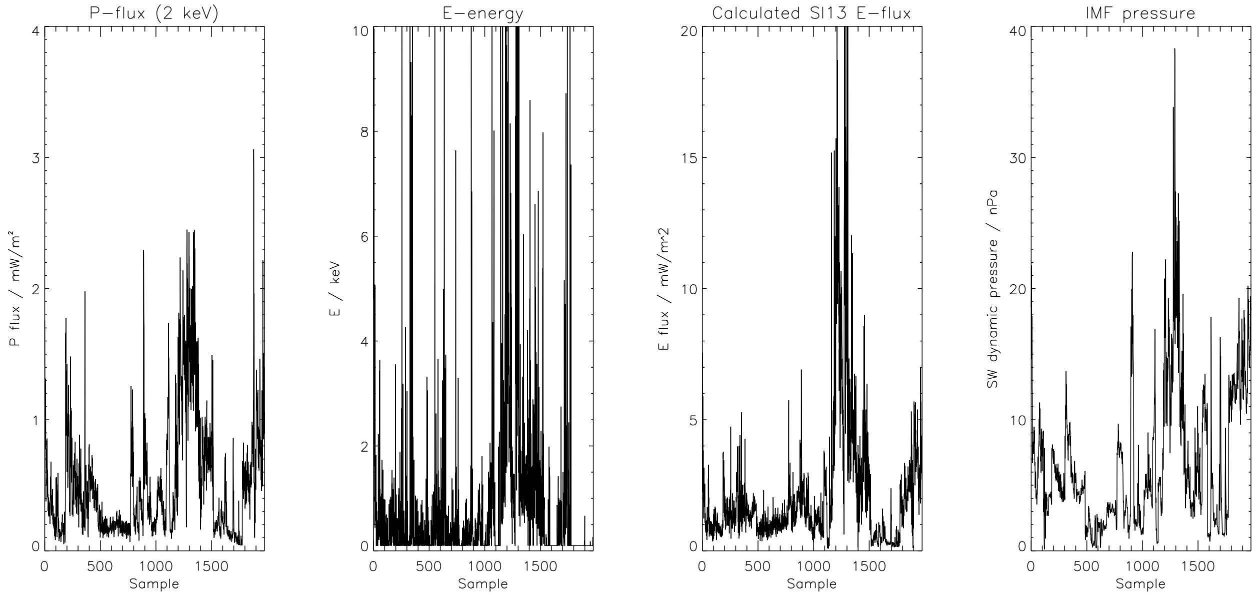

Fri Aug 31 14:46:31 2001, hfrey
/disks/sprite/disk1/hfrey/idl/image/fuview/mach_all_cusp_figures_newest

Figure 19

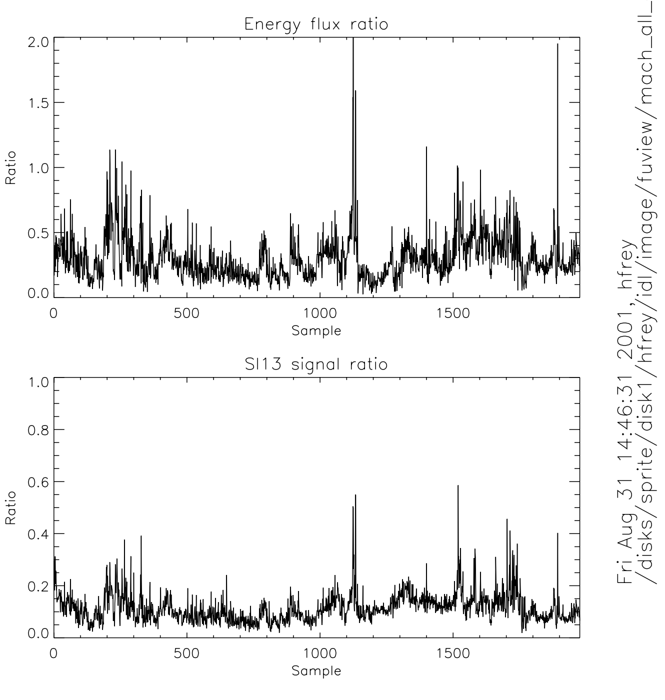
Energy flux ratio
Ratio
2.0
1.5
1.0
0.5
0.0
0
500
1000
1500
Sample
SI13 signal ratio
Ratio
1.0
0.8
0.6
0.4
0.2
0.0
0
500
1000
1500
Sample
Fri Aug 31 14:46:31 2001, hfrey
/disks/sprite/disk1/hfrey/idl/image/fuview/mach_all_cusp_figures_newest